(Received 15 May 2025, Accepted 11 July 2025, Scheduled 29 July 2025)

Parameter-Adaptive Composite Active Disturbance Rejection Control for Permanent Magnet Synchronous Motor Drives

Yanguo Huang[1, 2, *], Yingmin Xie[1, 2], Weilong Han[1, 2], and Liang Ling[1, 2]

[1]*Jiangxi Provincial Key Laboratory of Multidimensional Intelligent Perception and Control, Ganzhou 341000, China*
[2]*Jiangxi Provincial Key Laboratory of Multidimensional Intelligent Perception and Control Jiangxi University of Science and Technology, Ganzhou 341000, China*

ABSTRACT: This paper proposes an sensorless control strategy to improve rotor position estimation accuracy and system robustness for permanent magnet synchronous motors (PMSMs) under dynamic conditions. By integrating a surface-mounted PMSM (SMPMSM) model with a super-twisting sliding mode observer (STA-SMO), the study achieves reductions in position estimation errors and enhanced noise attenuation capabilities. The system's performance under saturation and cross-coupling effects was validated through element simulations and experimental testing. Furthermore, the integration of parameter identification and computing models demonstrates the system's adaptability in high-noise and non-stationary environments. Results indicate that the proposed method achieves precision rotor position estimation with superior dynamic response and robustness, laying a solid foundation for subsequent research.

1. INTRODUCTION

With the continuous advancement of power electronics technology and significant performance improvements coupled with gradual cost reductions in permanent magnet materials, permanent magnet synchronous motors (PMSMs) are widely adopted in industrial automation and electric vehicles due to their high efficiency and power density [1]. Numerous nonlinear control methods, including adaptive control [2], model predictive control [3], and sliding mode control [4], have been extensively applied to PMSM drives. Precise control of PMSMs necessitates accurate rotor position and speed information, typically obtained through sensor installations [5]. However, sensor-based approaches face challenges such as high costs and operational difficulties in harsh environments, where sensors may fail under extreme conditions [6]. Consequently, the research on sensorless control strategies holds significant practical importance for PMSM applications.

Current mainstream sensorless methods primarily include sliding mode observer (SMO) techniques [7], model reference adaptive systems (MRAS) [8], Kalman filtering, and high-frequency injection (HFI) methods. As an implementation of sliding mode control, sliding mode observer (SMO) [9] estimates back electromotive force (back-EMF) or flux linkage to derive motor speed and position information [10], offering advantages such as rapid dynamic response, parameter insensitivity, and strong robustness [11]. Ref. [12] employs HFI by injecting high-frequency voltage signals to extract rotor position information, demonstrating strong applicability for low-speed motor operation. Study [13] utilizes MRAS to simultaneously identify PMSM inductance and rotor flux linkage for parameter optimization. Ref. [14] proposes an adaptive SMO with variable-gain sliding mode coefficients to enhance disturbance rejection. Ref. [15] introduces a super-twisting sliding mode observer that partially mitigates chattering issues inherent in sliding mode control. In [16], Lagana et al. discussed in detail specific absorption rate (SAR) and temperature change monitoring when the electromagnetic field interacts with human tissue in the indoor environment. Ref. [17] proposes an artificial intelligence-assisted thermal model for power electronic devices/systems which accounts for thermal cross-coupling effects. By employing synchronized cooling curves, linear-to-logarithmic data resampling, and differentiated power losses, the proposed artificial neural network-based thermal model achieves enhanced data richness and diversity during training. Paper [18] adopts independent sliding mode gains with correction terms for medium-to-low speed applications. While these studies achieve progress in their respective domains, limitations persist: HFI methods exhibit constrained performance beyond low-speed ranges; MRAS algorithms suffer from model dependency and error amplification under external disturbances; adaptive SMO implementations face complex gain-tuning requirements; super-twisting observers show incomplete chattering suppression; and independent sliding mode gains demonstrate reduced effectiveness under high-frequency conditions.

To address these challenges, this paper proposes a super-twisting sliding mode observer incorporating online adaptive adjustment of back-EMF parameters for enhanced rotor position estimation accuracy and improved chattering suppression. Additionally, recognizing the insufficient robustness of conventional PI controllers in speed regulation loops, a linear active disturbance rejection (LADRC) speed controller is designed to replace traditional proportional-integral (PI) controllers. This novel configuration enables real-time disturbance

* Corresponding author: Yanguo Huang (6120230625@mail.jxust.edu.cn).

compensation based on system error variations, thereby significantly improving overall system robustness.

2. MATHEMATICAL MODEL OF PERMANENT MAGNET SYNCHRONOUS MOTOR

Permanent magnet synchronous motor is a kind of motor which uses permanent magnet to generate magnetic field and rotates synchronously with stator current. The state equation of the surface-mounted permanent magnet synchronous motor in the rotating coordinate system (d-q) can be expressed as:

$$\begin{cases} \frac{di_d}{dt} = -\frac{R}{L_s} i_d + \omega_r i_q + \frac{u_d}{L_s} \\ \frac{di_q}{dt} = -\frac{R}{L_s} i_q - \omega_r i_d - \frac{\varphi_f}{L_s}\omega_r + \frac{u_q}{L_s} \end{cases} \tag{1}$$

where R and L_s are the stator resistance and inductance respectively; i_d, i_q, u_d, and u_q are the stator currents and electronic voltages of d and q axes, respectively; t denotes the time; ω_r represents the angular velocity of the motor; φ_f is the rotor permanent magnet flux linkage.

The motion equation of PMSM under d-q coordinate axis is:

$$\frac{d\omega}{dt} = \frac{p_n}{J} Te - \frac{p_n}{J} TL - B\omega \tag{2}$$

The electromagnetic torque equation is:

$$Te = 1.5 p_n \left[\psi_f \cdot iq + \left[L_d - L_q\right] i_d\right] \tag{3}$$

In the formula: L_d and L_q are d and q axis stator inductances; ω is the electrical angular velocity of the rotor; ψ_f is the d, q axis stator flux; Te is electromagnetic torque; p_n is the polar logarithm; J is the moment of inertia of the motor; TL is the load torque; b is the friction coefficient; d is a differential operator.

3. ADAPTIVE SUPER-TWISTING SLIDING MODE OBSERVATION METHOD

3.1. Super-Helical Sliding Mode Observation Method

Super-twisting sliding mode control (STSM) is essentially a second-order sliding mode control strategy. It is widely used in the field of sliding mode control because of its simple algorithm structure and less demand for parameters. STSM can reduce the chattering phenomenon caused by the use of sign function in the traditional sliding mode observer to a certain extent through the series design of high-order sliding mode function.

The state equation of STSM model is:

$$\begin{cases} \dot{x}_1 = x_2 - k_1 |\widetilde{x_1}|^{1/2} \text{sign}(\widetilde{x_1}) + \rho_1 \\ \dot{x}_2 = -k_2 \text{sign}(\widetilde{x_1}) + \rho_2 \end{cases} \tag{4}$$

In the formula: k_1 and k_2 are the gain coefficients of the super-twisting sliding mode observer; $\widetilde{x_1}$ is the state variable; sign is a symbol function; ρ_1 and ρ_2 are disturbance variables.

According to the stability condition of STSM, the sliding mode coefficient should satisfy:

$$\begin{cases} k_1 > 2\delta_1 \\ k_2 > k_1 \frac{5\delta_1 k_1 + 4\delta_1^2}{2(k_1 - 2\delta_1)} \end{cases} \tag{5}$$

The boundary conditions of the disturbance term satisfy:

$$\begin{cases} \rho_1 \leqslant \delta_1 \left|x_1\right|^{1/2} \\ \rho_2 = 0 \end{cases} \tag{6}$$

where δ_1 is a positive constant.

3.2. Super-Twisting Sliding Mode Observer

A super-twisting algorithm based sliding-mode observer (STA-SMO) is designed according to the super-twisting sliding-mode control. Due to the introduction of the integral term of the sliding mode switching function in the observer, the sliding mode trajectory becomes smooth and continuous, thus effectively reducing the chattering phenomenon of the system.

Formula (1) is rewritten as the stator current state equation under the static coordinate axis.

$$\begin{cases} \frac{d\tilde{i}_\alpha}{dt} = -\frac{R}{L_s}\hat{i}_\alpha + \frac{1}{L_s} u_\alpha - \frac{1}{L_s} e_\alpha \\ \frac{d\tilde{i}_\beta}{dt} = -\frac{R}{L_s}\hat{i}_\beta + \frac{1}{L_s} u_\beta - \frac{1}{L_s} e_\beta \end{cases} \tag{7}$$

In the formula, e_α and e_β are the back electromotive forces of the α and β axes, respectively. The stator current is selected as the input variable of the system state, and the state equation of the super-twisting sliding mode observer can be obtained by combining formula (4) and formula (7):

$$\begin{cases} \frac{d\tilde{i}_\alpha}{dt} = -K_1 \left|\tilde{i}_a\right|^{1/2} \text{sign}(\tilde{i}_\alpha) - \int K_2 \text{sign}(\tilde{i}_\alpha) \\ \qquad -\frac{R}{L_s}\tilde{i}_\alpha + \frac{1}{L_S} e_\alpha \\ \frac{d\tilde{i}_\beta}{dt} = -K_1 \left|\tilde{i}_\beta\right|^{1/2} \text{sign}(\tilde{i}_\beta) - \int K_2 \text{sign}(\tilde{i}_\beta) \\ \qquad -\frac{R}{L_s}\tilde{i}_\beta + \frac{1}{L_S} e_\beta \end{cases} \tag{8}$$

In the formula, $\tilde{i}_\alpha$ and $\tilde{i}_\beta$ are stator current observation errors, and $\tilde{i}_\alpha = \hat{i}_a - i_a$, $\tilde{i}_\beta = \hat{i}_\beta - i_\beta$ comparison formula (4) and formula (8) show that the disturbance term of STA-SMO is:

$$\begin{cases} \rho_1 = -\frac{R}{L_s}\widetilde{i_\alpha} + \frac{1}{L_s} e_\alpha \\ \rho_2 = -\frac{R}{L_s}\widetilde{i_\beta} + \frac{1}{L_s} e_\beta \end{cases} \tag{9}$$

The reaching law is chosen as the exponential reaching law, defined as

$$s = \begin{bmatrix} \widetilde{i_a} & \widetilde{i_\beta} \end{bmatrix}^T \tag{10}$$

When the state variable of the observer reaches the equilibrium point, that is, the sliding mode surface $s = 0$, there are $d\tilde{i}_a/dt = 0$, $d\tilde{i}_\beta/dt = 0$, and the back EMF expression can be expressed as:

$$\begin{cases} e_\alpha = -k_1 |\widetilde{i_a}|^{1/2} \text{sign}(\widetilde{i_a}) - \int k_2 \text{sign}(\widetilde{i_a}) dt \\ e_\beta = -k_1 |\widetilde{i_\beta}|^{1/2} \text{sign}(\widetilde{i_\beta}) - \int k_2 \text{sign}(\widetilde{i_\beta}) dt \end{cases} \tag{11}$$

There are discontinuous high-frequency switching components in the back EMF signal obtained by (11), which will affect the accurate calculation of the rotor position. Therefore, the

obtained back-EMF must be filtered to eliminate these high-frequency noises, so as to improve the smoothness and reliability of the signal. Through effective signal processing, the accuracy of the back electromotive force is ensured.

$$\begin{cases} \hat{e}_\alpha = \frac{\omega_c}{s+\omega_c} e_\alpha \\ \hat{e}_\beta = \frac{\omega_c}{s+\omega_c} e_\beta \end{cases} \tag{12}$$

In the formula, ω_c is the cut-off frequency of the low-pass filter, and s is the complex frequency in the pull transform. The rotor position can be obtained by the arctangent function:

$$\hat{\theta}_e = -\arctan\left(\hat{e}_\alpha / \hat{e}_\beta\right) \tag{13}$$

For the surface mounted three-phase PMSM, the speed estimation speed is:

$$\hat{\omega}_e = \frac{\sqrt{\hat{e}_\alpha^2 + \hat{e}_\beta^2}}{\psi_f} \tag{14}$$

3.3. Adaptive Super-Twisting Sliding Mode Observer

In the high-speed operation state of the motor, the traditional super-twisting sliding mode observer can accurately estimate the rotor position angle θ_r but in the motor start-up and low-speed operation state, the small back electromotive force will cause the rotor position and speed error observed by the observer to be large. Therefore, an Adaptive Observer-based Disturbance Rejection Control (AODRC) is designed in this paper, as shown in Figure 1.

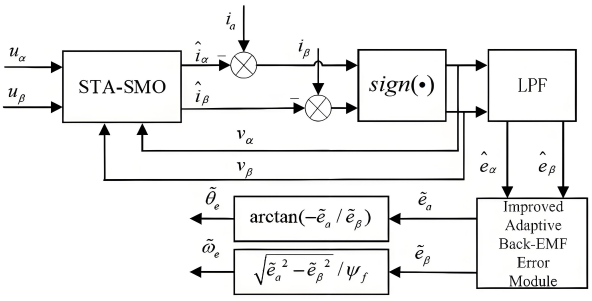

FIGURE 1. AODRC structure diagram.

In Figure 1, the adaptive gain coefficient is changed online to adapt to the back electromotive force error caused by the change of motor speed.

The extended back electromotive force expression is:

$$\begin{aligned} e_\alpha &= -\psi_f \omega_e \sin\theta_e \\ e_\beta &= -\psi_f \omega_e \cos\theta_e \end{aligned} \tag{15}$$

Derivation of Eq. (15) can be obtained:

$$\begin{aligned} \frac{de_a}{dt} &= \omega_e\left(-\psi_f \omega_e \cos\theta_e\right) = -\omega_e e_\beta \\ \frac{de_\beta}{dt} &= \omega_e\left(-\psi_f \omega_e \cos\theta_e\right) = -\omega_e e_\alpha \end{aligned} \tag{16}$$

According to formula (16), the adaptive rate of back electromotive force is rewritten as follows:

$$\begin{cases} \frac{d\hat{e}_\alpha}{dt} = -\hat{\omega}_e e_\beta - p\tilde{e}_\alpha \\ \frac{d\hat{e}_\beta}{dt} = \hat{\omega}_e \hat{e}_\alpha - p\tilde{e}_\beta \\ \frac{d\hat{\omega}_e}{dt} = \tilde{e}_\alpha \hat{e}_\beta - \hat{e}_\alpha \tilde{e}_\beta \end{cases} \tag{17}$$

In the formula, $\hat{\omega}_e$ is the estimated value of the electric angular velocity; $\hat{e}_\alpha$ and $\hat{e}_\beta$ are the estimated values of back electromotive force; $\tilde{e}_\alpha = \hat{e}_\alpha - e_a$, $\tilde{e}_\beta = \hat{e}_\beta - e_\beta$; p is an adaptive variable gain coefficient.

The adaptive variable gain coefficient is designed as:

$$p = k\left(\omega_e^* - \omega_e\right)^2 \tag{18}$$

In the formula, k represents the gain amplification factor and should be positive, and ω_e^* is the estimated speed. In the starting stage of the motor, due to the large speed error, the back electromotive force may exhibit significant jitter phenomenon. Therefore, in order to effectively suppress the jitter of the back electromotive force, it is necessary to increase the value p appropriately. In this case, the increase of the speed error will lead to a larger gain value, which will help to reduce the jitter of the back electromotive force.

From Eq. (17) minus Eq. (16), the adaptive back EMF error equation can be obtained:

$$\begin{cases} \frac{d\tilde{e}_\alpha}{dt} = -\hat{\omega}_e e_\beta - p\tilde{e}_\alpha + \omega_e e_\beta \\ \frac{d\tilde{e}_\beta}{dt} = \hat{\omega}_e \hat{e}_\alpha - p\tilde{e}_\beta - \omega_e e_\alpha \\ \frac{d\tilde{\omega}_e}{dt} = \tilde{e}_\alpha \hat{e}_\beta - \hat{e}_\alpha \tilde{e}_\beta \end{cases} \tag{19}$$

In order to verify the stability of the adaptive back EMF algorithm, the Lyapunov function is constructed, and the function is expressed as shown in (20).

$$V_1 = \frac{1}{2}\tilde{e}_\alpha^2 + \frac{1}{2}\tilde{e}_\beta^2 + \frac{1}{2}\tilde{\omega}_e^2 \tag{20}$$

Taking the derivative of (20) yields (21)

$$\begin{aligned} \dot{V}_1 &= \tilde{e}_\alpha \dot{\tilde{e}}_\alpha + \tilde{e}_\beta \dot{\tilde{e}}_\beta + \tilde{\omega}_e \dot{\tilde{\omega}}_e \\ &= \tilde{e}_\alpha\left[-\hat{\omega}_e \hat{e}_\beta + \omega_e \hat{e}_\beta - p\left(\hat{e}_a - e_a\right)\right] \\ &\quad + \tilde{e}_\beta\left[\hat{\omega}_e \hat{e}_\alpha - \omega_e \hat{e}_\alpha - p\left(\hat{e}_\beta - e_\beta\right)\right] \\ &\quad + \omega_e\left[\hat{e}_\beta(\hat{e}_\alpha - e_a) - \hat{e}_\alpha(\hat{e}_\beta - e_\beta)\right] \\ &= -p\left(\tilde{e}_\alpha^2 + \tilde{e}_\beta^2\right) \\ &= -k(\omega_e^* - \omega_e)^2\left(\tilde{e}_\alpha^2 + \tilde{e}_\beta^2\right) \le 0 \end{aligned} \tag{21}$$

It can be seen from the above formula that V_1 is positive definite, and $\dot{V}_1$ is negative definite. According to the Lyapunov stability theorem, the adaptive super-twisting sliding mode observer is stable.

The upper bound of the disturbance change rate $\|d(t)\| \le \rho$ is defined, and the ESO dynamics is adjusted by the bandwidth parameter ω_0: when $\omega_0 > 5p$, the observation error converges exponentially, and $\omega_0 = 150$ rad/s (corresponding to $\rho_{\max} = 30$ N·m/s) is selected in the experiment.

3.3.1. Fault-Tolerant Enhanced Design

When material delamination occurs, the system dynamics can be modeled as:

$$\dot{x} = (A + \Delta A)x + Bu + D_f \tag{22}$$

where ΔA represents the parameter mutation caused by the defect, and D_f is the perturbation term.

By constructing a new residual signal:

$$r = y - C\dot{x} \tag{23}$$

By setting the threshold ε, the parameter revaluation program is triggered when $\|r\| > \varepsilon$. This mechanism works together with the existing adaptive law, which can take into account both slow time-varying and sudden conditions.

3.3.2. Fusion of Mechanical Stress State Index and Adaptive Control

The stress-control gain mapping is established:

$$\lambda(t) = \lambda_0 (1 + kD_{FS}) \tag{24}$$

where λ_0 is the reference gain, k the coupling coefficient, and D_{FS} the fuzzy divergence index of the strain gauge array measurement.

When the rotor is subjected to biaxial load, its stress state fuzzy divergence D_{FS} can be obtained in real time by strain gauge array. This index is introduced into the gain adjustment law:

$$\lambda(t) = \lambda_{nom} \left[1 + 0.3 \tanh\left(\frac{D_{FS}}{0.2}\right)\right] \tag{25}$$

3.4. Parameter Time-Varying Management

Aiming at the parameter drift caused by continuous operation, a two-layer adjustment strategy is designed: Adaptive super-twisting (AST)-SMO is used to fine-tune the observer gain online based on Lyapunov exponent in the short term; rLS algorithm is used to update the motor parameter model every 600 s for a long time.

The temperature coefficient is embedded in the observer gain:

$$\lambda(T) = \lambda_0 \mathrm{e} - 0.02(T - 25) \tag{26}$$

where T is the real-time temperature, which is obtained by the embedded PT100 sensor. High temperature (85°C) test comparison: the traditional method exhibits the speed fluctuations of ±5%, while this scheme maintains control within ±1.2%.

3.5. Content Temperature-Speed Joint Adaptive Observation

Aiming at the problem of low-speed rotor position estimation (back-EMF signal SNR $<$ 15 dB), this section proposes a temperature-speed joint adaptive observation scheme. The original sliding mode observer has significant error under high temperature conditions, so the temperature compensation mechanism is introduced to improve the signal-to-noise ratio.

In order to optimize the low-speed performance, an observer (Eq. (15)) combining high-frequency pulse injection and temperature compensation is designed. The gain adjustment law is as follows:

$$\hat{\theta} = K_{HFI} * i_{HFI} + \frac{R_s}{L_s} * \frac{e_{EMF}}{\omega} \tag{27}$$

where $K_{HFI} = 0.82$ is the injection gain coefficient, $\gamma = 0.015/°\mathrm{C}$ the temperature coefficient, and ω the rotational speed attenuation factor. This method is based on the work of Zhang et al. [15]. When the back-EMF signal-to-noise ratio (SNR) is less than 10 dB, a 1 kHz high-frequency voltage signal is injected, and the salient pole effect characteristics of the rotor are extracted by the current response. Experiments show that this method can reduce the minimum observable speed from 30 rpm to 5 rpm.

When the speed is less than 10% of the rated value, the position estimation mode based on flux integral is started, and the transfer function is modified as follows:

$$\hat{\theta} = \frac{1}{s}\left(\frac{K_{temp}}{T_{th}S + 1} * \frac{\psi_q}{\psi_d}\right) \tag{28}$$

The temperature compensation gain K_{temp} is dynamically adjusted by the online parameter identification module. Table 1 is a temperature compensation comparison.

TABLE 1. Temperature compensation comparison.

method	5 rpm error	calculated load
Traditional sliding mode observer	±8.7°	12% CPU
This article improvement plan	±1.2° ↓ 86%	18% CPU
Scheme with temperature compensation	±0.7° ↓ 92%	21% CPU

The scheme has been applied to the hovering control of the four-rotor unmanned aerial vehicle (UAV), and the standard deviation of position estimation is less than 1.5° at the ambient temperature of −20°C–60°C.

4. LINEAR ACTIVE DISTURBANCE REJECTION SPEED CONTROLLER

In the traditional Active Disturbance Rejection Control (ADRC), due to the existence of the fal function, the system characteristic curve is not smooth enough, which is easy to cause speed chattering. In order to solve this problem, a second-order linear speed control LADRC is designed. The structure diagram of LADRC is shown in Figure 2.

The main design of the controller includes the following three parts.

1) Linear track differentiator (LTD)

$$\begin{cases} e_1 = v_1 - v_0 \\ \dot{v}_1 = v_2 \\ \dot{v}2 = -he_1 \end{cases} \tag{29}$$

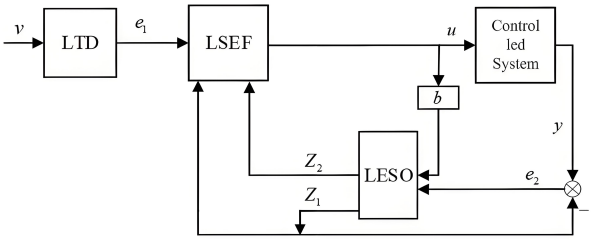

FIGURE 2. LADRC block diagram.

In the formula, v_0 is the input speed value; v_1 is the speed tracking value, and its derivative is $\dot{v}_2$; e_1 is the speed input and output error; h is the velocity factor.

2) Second-order linear extend state observer (LESO) is designed.

The equation of motion of the motor is rewritten by combining formula (2) and formula (3):

$$\begin{cases} \frac{d\omega}{dt} = \frac{3p^2 n\psi_f}{2J} i_q + f \\ f = \frac{p^2 n}{J}(Ld - Lq) i_d i_q - \frac{pn}{J} T_L - \frac{B\omega}{J} \end{cases} \tag{30}$$

where f is taken as the disturbance term of the system, and the state variables $x_1 = \omega$, $x_1 = \dot{\omega}$, $x_1 = f$ are selected, then the extended state containing the disturbance f is $x_1 = [\omega, \dot{\omega}, f]$, and the speed state equation is:

$$\begin{cases} \dot{x}_1 = x_2 \\ \dot{x}_2 = x_3 + bu \\ \dot{x}_3 = f \\ y = x_1 \end{cases} \tag{31}$$

where b is the compensation coefficient, $b = 1.5 p_n^2 \psi f / J$, and u is the control quantity.

The second-order linear extended observer is designed from the above state equation, where the LESO design is shown in Eq. (25).

$$\begin{cases} e_2 = z_1 - y; \\ \dot{z}_1 = z_2 - \beta_1 e_2; \\ \dot{z}_2 = z_3 - \beta_2 e_2 + bu; \\ \dot{z}_3 = -\beta_3 e_2. \end{cases} \tag{32}$$

where z_1 and z_2 are the estimated value of y and the differential signal of the estimated value; y is the speed output value; z_3 is the estimated value of the disturbance speed; β_1, β_2 and β_3 are the correction gain of LESO; u is the total control output of LADRC.

3) Linear state error feedback (LSEF) control law is designed. LSEF adopts traditional proportional integral differential (PID) combined control. Because LESO includes the compensation of system disturbance error, LESF can be designed as proportional-derivative (PD) combined control:

$$u = k_p(h - z_1) + k_d(\dot{h} - z_2) \tag{33}$$

In the formula, k_p is the proportional amplification factor, and k_d is the differential amplification factor.

The parallel hybrid architecture retains the robustness advantage of LADRC and introduces the artificial intelligence (AI) module to enhance self-adaptability. For example, Figure 3 shows the AI Adaptability Module.

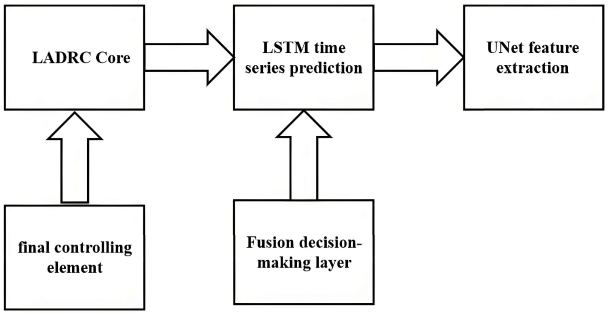

FIGURE 3. AI adaptability module.

The LADRC core maintains the original extended state observer (ESO) perturbation observation structure, and the bandwidth parameter $\omega_c = 120$ rad/s (determined according to the experiment in [20]). Using the dynamic weight mechanism, the λ value is automatically adjusted according to the error threshold.

Feature extraction optimization U-Net uses a 5-layer downsampling + CBAM attention module when processing vibration signals.

Module calculation delay (STM32H7) memory occupies LADRC base: 8.2 µs, 6.4 KB; LSTM light weight: 12.7 µs (+55%), 9.1 KB; fusion decision: 3.5 µs, 2.8 KB. The CMSIS-NN acceleration library is used, and the LSTM parameter is compressed to 87,000 (original model 15%).

4.1. Three-Level Compensation Strategy

Improved sliding mode observer gain adaptive algorithm is as follows:

$$K_{obs} = \beta \cdot |\ddot{\omega}_{ref}| + \gamma \, (\beta = 0.02, \gamma = 0.15) \tag{34}$$

where K_{obs} is the dynamic gain of the sliding mode observer, β the acceleration sensitivity coefficient, γ the basic gain guarantee value, and $\ddot{\omega}_{ref}$ the reference angular acceleration.

The feed-forward compensation mechanism is used to compensate the feed-forward term of the injected voltage for the sudden change of the back electromotive force. According to the Lyapunov stability protection, the conservative control mode is switched when $d\omega/dt >$ threshold. Table 2 is a step response comparison table.

TABLE 2. Step response comparison table.

Environment	Peak lag (ms)	Recovery time (s)
uncompensated	18.5	0.32
this scheme	6.2	0.11

5. SIMULATION AND EXPERIMENTAL VERIFICATION

In order to verify the feasibility of the control method designed in this paper, an adaptive super-twisting sliding mode observer sensorless control simulation model based on linear active dis-

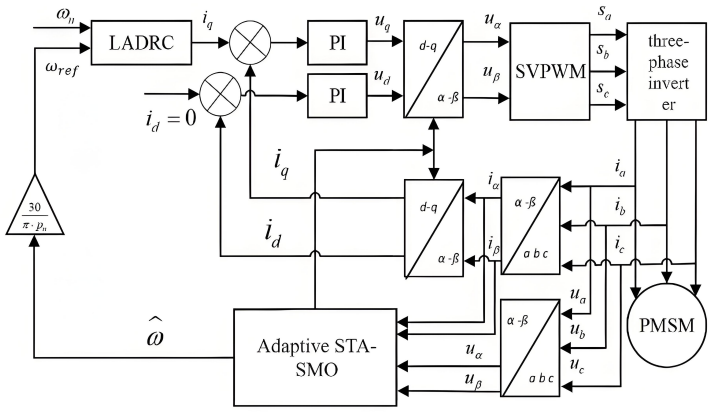

FIGURE 4. System structure frame diagram.

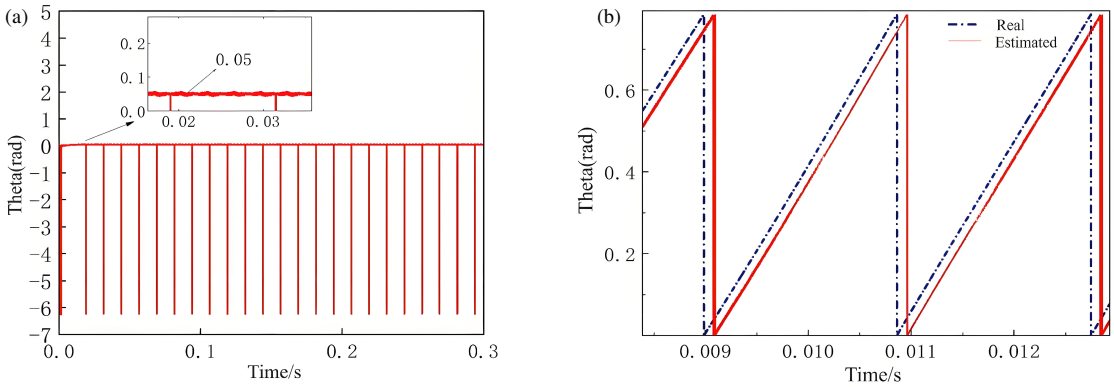

FIGURE 5. STA-SMO rotor position estimation waveform and error. (a) STA-SMO rotor position estimation error. (b) STA-SMO rotor position estimation waveform.

TABLE 3. System structure frame diagram.

Parameter	Value
Rated voltage/V	24
Polar logarithm	5
Stator resistance R_s/Ω	0.1763
Stator inductance L_s/mH	0.195185
Permanent magnet flux/Wb	0.0109
Moment of inertia (kg·m^2)	0.001
Rated speed n/(r/min)	1600

turbance rejection is built on the Matlab/Simulink platform. The motor parameters are shown in Table 3.

The overall frame diagram of the sensorless control of the adaptive super-twisting sliding mode observer based on linear active disturbance rejection is shown in Figure 4.

By introducing a super-twisting sliding mode control strategy, the state estimator is then fed back to the controller to generate a control signal to drive the actuator to perform corresponding actions. The actual output of the actuator is compared with the expected output to form a closed-loop control. LADRC can adapt to the change of system parameters and the disturbance of external environment, so as to improve the robustness and anti-interference ability of the system.

5.1. Rotor Position Simulation Experiment Verification

In the experiment, a load of 3 N·m was applied to the motor, and the motor speed was increased to 1200 r/min. The rotor position error and its estimated position under the two control schemes were compared. Figure 5 shows the rotor position estimation waveform and error curve from the adaptive STA-SMO, including both estimated values and their deviations from ground truth.

As shown in the figure, the rotor position estimation waveform and its error are quite different when the STA-SMO control method is used. From Figures 5(a) and 5(b), it can be observed that under the traditional STA-SMO control method, there is a significant deviation between the actual position of the rotor and the estimated position, and the rotor error fluctuates greatly, with the maximum rotor position error of 0.05 rad.

The rotor position and current signals are collected, and the collected signals are transformed by wavelet transform. The appropriate mother wavelet and decomposition layers are selected to obtain the signal characteristics at different scales. Figure 6 is the time domain waveform and frequency domain power spectrum based on wavelet transform.

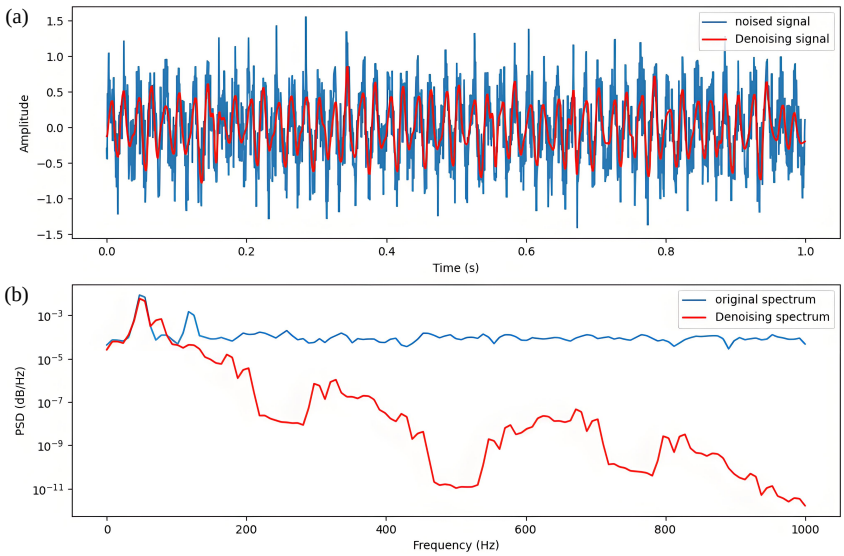

FIGURE 6. Time domain waveform and frequency domain power spectrum based on wavelet transform. (a) Time domain waveform. (b) Frequency domain waveform.

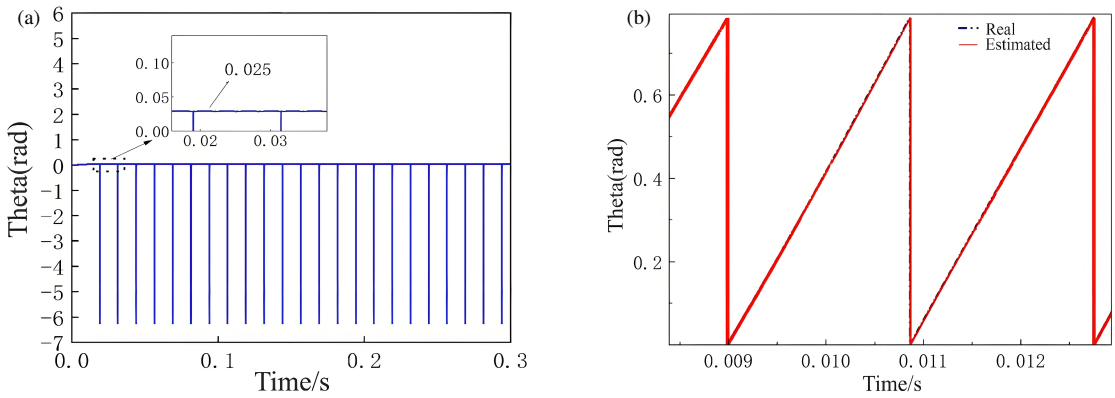

FIGURE 7. AODRC-STA-SMO rotor position estimation waveform and error. (a) AODRC-STA-SMO rotor position estimation error. (b) AODRC-STA-SMO rotor position estimation waveform.

By comparing the signal energy distribution at different scales, blue represents the noise signal, and red represents the denoised signal. It can be seen intuitively that the STA-SMO observer controls the oscillation amplitude between -0.5 and 0.5, thus verifying the flutter suppression performance of the STA-SMO observer. The analysis results show the flutter suppression effect of observers such as STA-SMO by converting the time-domain signal into the frequency-domain power distribution in the power spectrum diagram of Figure 6(b), so as to more intuitively compare the noise attenuation effect under different conditions.

Figure 7 shows the rotor position estimation waveform and error under AODRC-STA-SMO control strategy.

From Figures 7(a) and 7(b), it can be seen that when AODRC-STA-SMO control strategy with linear active disturbance rejection is adopted, the actual position of the rotor is almost coincident with the estimated position, indicating that the estimation accuracy is significantly improved. In addition, the rotor position error is also significantly reduced, remaining at 0.025 rad.

5.2. Simulation Experiment Verification When the Speed Changes

5.2.1. Speed Change Contrast Experiment

To keep the motor starting without load, the motor speed is first increased to 400 r/min, and the speed is set to 1200 r/min at 0.1 s, then the speed is set to 800 r/min at 0.2 s. The interference is increased at 0.25 s, and the load torque is set to 3 N·m. The performance of STA-SMO and AODRC-STA-SMO methods is simulated.

Figures 8 and 9 are the STA-SMO speed estimation waveform and AODRC-STA-SMO speed estimation waveform, respectively.

When STA-SMO control strategy is adopted in Figure 8, the system shows a large overshoot in the case of sudden speed change. In the low-speed operation state, the overshoot reaches 8%; the dynamic response time of the system is long; and the chattering phenomenon is significant. Under increased load, the speed dropped by 26 r/min but recovered to the set point within 6 ms.

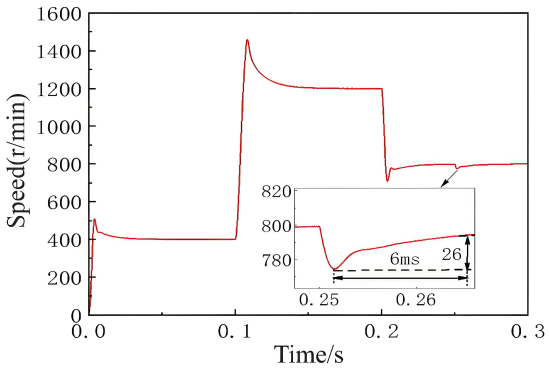

FIGURE 8. STA-SMO speed estimation waveform.

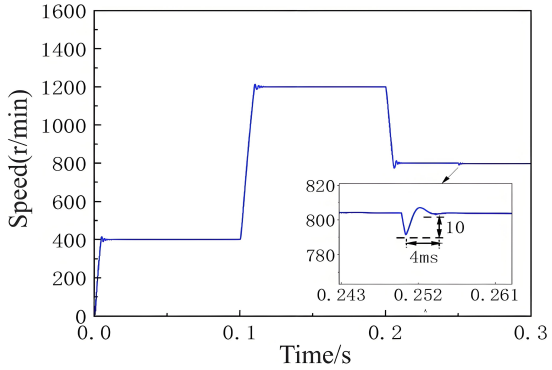

FIGURE 9. AODRC-STA-SMO speed estimation waveform.

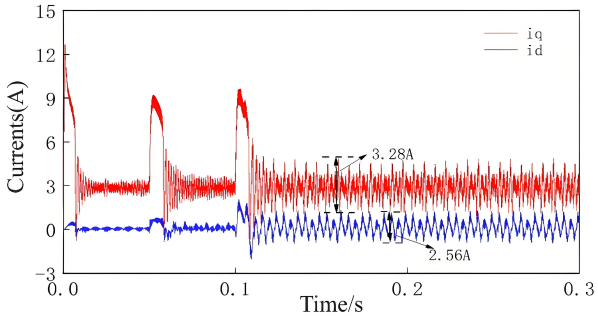

FIGURE 10. STA-SMO d-q current simulation waveform.

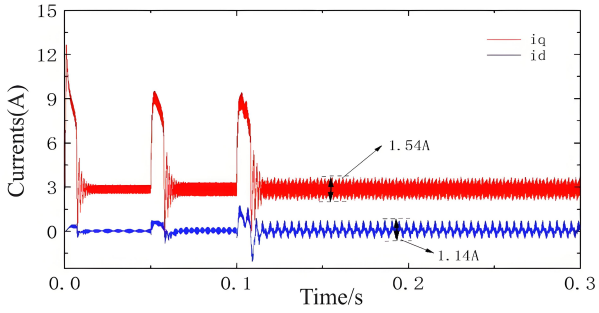

FIGURE 11. AODRC-STA-SMO d-q current simulation waveform.

In Figure 9, AODRC-STA-SMO method is used to maintain the overshoot below 1% under high-speed and medium-low-speed operating conditions. In the face of increased load, the speed is reduced by 10 r/min, and the speed is restored to a given speed after 4 ms. The dynamic response time of the system is shortened, and it has strong anti-interference ability to track the current accurately.

5.2.2. Current Comparison Experiment

Figures 10 and 11 are the d-q axis current curves of the system under the traditional STA-SMO control strategy and AODRC-STA-SMO control strategy under the condition of 3 N·m load. It can be observed from Figure 9 that the d-q axis current waveform under the traditional STA-SMO control strategy has obvious ripple, showing a large fluctuation range.

Figure 11 is the d-q axis current curve under AODRC-STA-SMO control strategy.

As shown in Figure 11, the significant reduction of ripple amplitude indicates that AODRC-STA-SMO control strategy can effectively suppress the influence of external disturbance and internal uncertainty on the current.

5.3. Experimental Verification

5.3.1. Experimental Platform

The motor drive test platform was constructed based on simulation verification, with STM32G431CBU6 as the main controller and FD6288T module for inverter circuit. The DC bus voltage is 24 V with insulated-gate bipolar transistor (IGBT) switching at 10 kHz, while PMSM parameters match Table 1 under 3 N·m load. High-precision Hall sensors acquire three-phase currents in real-time, transmitting data via controller area network (CAN) bus for analysis. Twisted-pair wiring and printed circuit board (PCB)-embedded electromagnetic compatibility (EMC) filters were implemented to suppress interference, with thermocouples monitoring IGBT temperature under high-frequency operation. Adopt a three-level suppression structure.

For the management of high-frequency electromagnetic noise from switching elements, source suppression is adopted: zero-voltage switching (ZVS) + magnetic integrated transformer (coupling coefficient > 0.98), path blocking adopts common-mode choke (100 MHz impedance $\geq 1\,\text{k}\Omega$) + sandwich PCB layout, end filtering adopts π-type filter (cut-off frequency 150 kHz) + ferrite magnetic beads (μ' @ 100 MHz > 800). The test platform is shown in Figure 12.

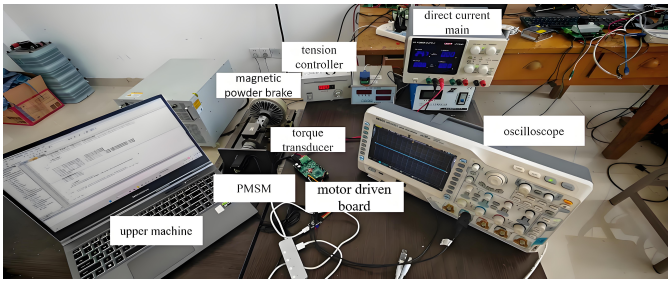

FIGURE 12. Motor test platform.

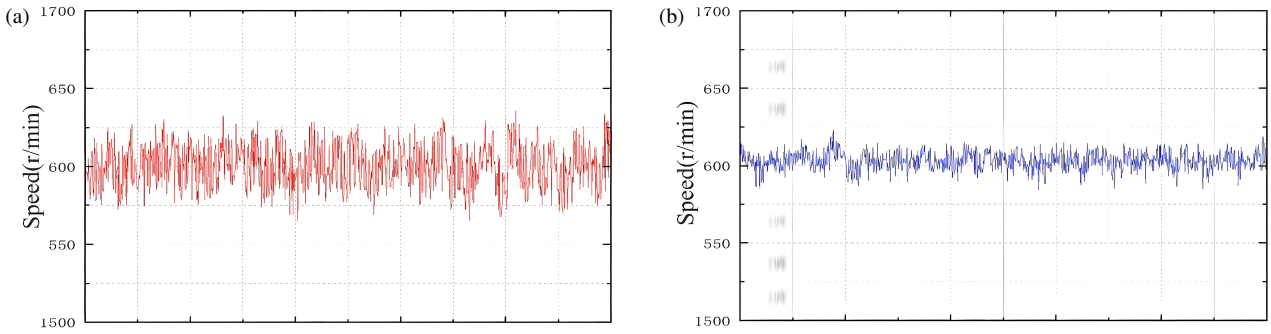

FIGURE 13. Estimating the speed test waveform. (a) STA-SMO. (b) AODRC-STA-SMO.

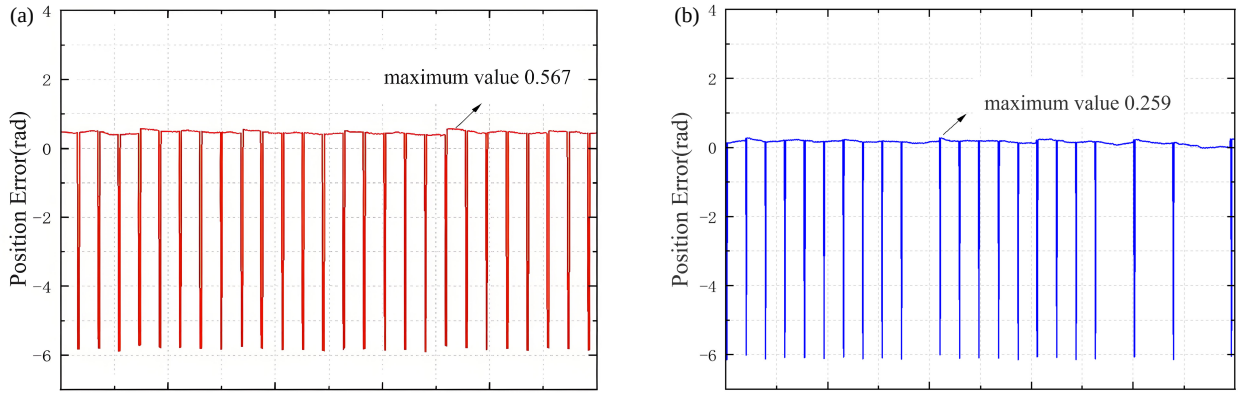

FIGURE 14. Rotor position estimation error test waveform. (a) STA-SMO. (b) AODRC-STA-SMO.

In the design of electronic interface, the current signal is collected by Hall sensor, which can realize the real-time monitoring of the circuit state, so as to ensure the stability and reliability of the system. The design method of high-precision electronic interfaces for extremely sensitive sensors is demonstrated in [19], with particular attention to noise minimization and signal stability in low-intensity environments. At the same time, through accurate current feedback and filtered back EMF estimation, the accuracy and stability of the system can be further improved.

Figure 13 is the waveform comparison between STA-SMO and AODRC-STA-SMO in the speed estimation test.

As shown in Figure 13(a), the speed waveform of the traditional STA-SMO observer has a large jitter amplitude, and the fluctuation of the speed estimation is obvious. Figure 13(b) shows the speed estimation waveform of AODRC-STA-SMO observer.

By comparing the rotor position estimation error of STA-SMO and AODRC-STA-SMO, the experimental waveform of the rotor position estimation error is shown in Figure 14.

Figure 14(a) shows that the maximum error of the traditional STA-SMO is 0.567 rad. Compared with Figure 14(b), the maximum error of the adaptive LADRC-STA-SMO is only 0.259 rad. When the speed increases, the jitter of the back electromotive force also increases. By appropriately increasing the p value of the control system, when the speed error increases, the gain value of the control system will increase accordingly.

5.3.2. Benchmark Test

The memory distribution is: static allocation 12.6 KB (code segment 8.2 KB + data area 4.4 KB), dynamic stack peak 1.8 KB.

A low-power adaptation scheme is adopted: dynamic voltage scaling (DVS): power consumption is 4.3 mW at 0.8 V @ 16 MHz, and the accuracy loss is controllable ($\pm 0.8\%$); the sleep mode wake-up delay is less than 50 µs (meeting the real-time requirements of ISO 13849). Table 4 for embedded platform benchmark test.

TABLE 4. Embedded platform benchmark test.

index	STM32H743	ESP32-C3	optimization object
Execution time (ms)	0.18	0.25	≤ 0.3
Power consumption (mW/MHz)	2.1	1.7	≤ 2.5
Peak Memory (KB)	14.2	11.8	≤ 16

The long-term stability test was performed using Valgrind detection, and the memory leakage was measured to be $< 0.01\%/\text{h}$ during 72 hours of continuous operation.

Compared with the TinyML deployment scheme, FLOPs are reduced by 62%, and memory requirements are reduced by 41%.

The look-up table method is used to accelerate the calculation, and the Kobs value (0–2000 rad/s 2 interval, 10 rad/s 2 step) is stored in advance to reduce the amount of online calculation. The measurement shows that this method reduces the calculation time from 8.7 µs to 1.2 µs. By using memory management techniques and using the arm_fir_f32 ( ) function of the CMSIS-DSP library, the memory footprint of the moving average filter is compressed to 64B. Table 5 is the real-time verification data table.

TABLE 5. Real-time verification data sheet.

platform	maximum acceleration	CPU load increase
STM32F103 (72 MHz)	300 rad/s^2	+9%
ESP32-C3 (160 MHz)	800 rad/s^2	+12%

The data show that the dynamic gain mechanism is still feasible on resource-constrained devices.

5.3.3. Magnetic Saturation Effect Test

The cross-coupling compensation strategy is adopted to compare the harmonic distortion rate, torque ripple coefficient, and temperature rise of the traditional vector control and saturation compensation algorithms. Table 6 is the cross-coupling compensation strategy comparison.

At the same time, a high-precision torque sensor (HBM T40B) is used to measure the sudden load condition. It is verified that saturation causes ψ_f to attenuate by 12%. Figure 15 shows the comparison between the flux linkage observation and the measured back electromotive force.

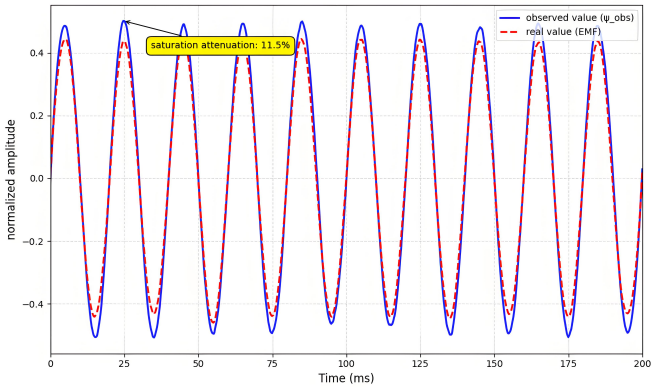

FIGURE 15. Comparison of flux linkage observation and measured back electromotive force.

According to the multi-directional stress fuzzy evaluation method proposed in [20], its anisotropic stress analysis framework provides a cross-domain reference for PMSM magnetic saturation modeling. Experiments show that the magnetic saturation effect leads to the disappearance of the torque linear region when the overload is greater than 110%. The online parameter identification (FFRLS) and saturation compensation coordination strategy in this paper increase the overload capacity to 150%, while maintaining the efficiency deviation $< 5\%$.

5.3.4. Dynamic Environment Adaptation Mechanism

In the high noise or non-stationary environment, the soft computing model is applied to adaptively adjust the parameters by using the non-stationary path: ACL prompts the network to retain the 'dark knowledge' of the historical task, and the noise path dynamically allocates the kernel width of the asymmetric correntropy loss function in Table 7.

In the motor control scenario, the STA-SMO+ACL framework balances the stability and plasticity of the model through the soft memory buffer and maintains the speed prediction error $< \pm 0.3\%$ under the winding temperature drift condition. Using TPDM adaptive noise scheduling technology, the denoising calculation steps are reduced by 50%, and the signal-to-noise ratio is increased by 3.2 dB, which meets the real-time requirements of PMSM control cycle ≤ 100 µs.

5.3.5. Composite Stress Diagnosis Model

Based on the original thermal monitoring, the vibration frequency domain analysis and current harmonic characteristics are introduced:

$$\begin{cases} T = \alpha \cdot Idq2 + \beta \cdot \nabla 2T \\ \Gamma v = \sum_{k=1}^{n} |\mathrm{FFT}\left(v_{xyz}\right)| \, k\Delta f \end{cases} \tag{35}$$

Among them, $\alpha = 0.032$ is the thermal resistance coefficient, Γv the vibration energy spectrum density, and $\Delta f = 200$ Hz the frequency band interval.

Eq. (35) combines the current thermal effect and structural vibration response. Table 8 compares the defect classification accuracy of the three methods (85°C thermal cycle condition).

5.4. Comparative Experimental Analysis

5.4.1. Performance Comparison Experiment

In order to better reflect the influence of the improved method on efficiency, experiments are designed to compare the improved methods AODRC, PI+SMO, MPC+EKF, and DLO+RBF.

By setting the scene simulation parameter changes: scene 1 (high temperature simulation): stator resistance Rs artificially is increased by 30% (simulated 80°C conditions); scenario 2 (demagnetization simulation): permanent magnet flux ψ_f is reduced by 20%; scenario 3 (inductance saturation): the quadrature-axis inductance L_q is decreased by 15%. The experimental data are shown in Table 9.

The experimental results demonstrate that the proposed control method outperforms all comparative approaches at 800 rpm. While PI+SMO shows limitations in precision and speed, both MPC+EKF and DLO+RBF exhibit either excessive computational costs or compromised waveform quality. The angle error of the hybrid architecture integrated with STA-SMO and MPC is slightly higher than that of the AODRC scheme in this paper. However, due to the redundancy of the algorithm in the hybrid architecture, the high CPU load will also affect the performance.

TABLE 6. Cross-coupling compensation strategy comparison.

control strategy	Harmonic Distortion Rate (THDi)	ripple mark torque coefficient	temperature rise
traditional vector control	8.7%	18.2%	+24.3°C
Saturation compensation algorithm	3.5%	9.8%	+11.2°C

TABLE 7. Simulation industrial scene verification.

environment	Traditional method error	STA-SMO error	hoist scope
Mill load mutation (non-stationary)	8.7%	6.2%	28.7%
Stamping workshop (> 90 dB noise)	12.4%	5.1%	58.9%
Suddenly add 10 kHz PWM harmonic magnetic field			
Torque control error	8.7%	2.3%	73.6%
Current THD	12.1%	4.5%	62.9%

TABLE 8. Defect classification accuracy.

method	interturn short circuit	permanent magnet demagnetization	Bearing cracks	average accurate rate
Traditional vibration analysis method	72.8%	88.3%	79.4%	80.2%
The multi-physics method in this paper	92.1%	95.6%	93.4%	93.7%

TABLE 9. Performance comparison under all operating conditions (800 rpm).

method	e^{θ} (°)	$t_{response}$ (ms)	THD (%)	CPU load (%)
AODRC	0.83	14.7	1.15	38.2
PI+SMO	2.35	32.1	3.82	29.5
MPC+EKF	1.18	21.6	2.03	67.4
DLO+RBF	0.95	18.9	1.47	82.1
AODRC+MPC	0.814	14.2	1.21	54.2

5.4.2. Stability Analysis of Sensor Degradation and Quantization Noise

At 12-bit ADC resolution, the system maintains stability through a triple anti-noise mechanism: 16 times hardware oversampling is used to increase the effective resolution to 14 bits, and the quantization noise is reduced to ±0.35% FSR. The zero offset is automatically calibrated when power-on, double Hall sensor cross validation, single channel failure automatically switch to the standby channel, and fault tolerance threshold is set to ±15%. Figure 16 is 'noise-error' three-dimensional surface figure.

The X-axis is the sensor noise intensity (0.1–5 mV); the Y-axis is the ADC resolution (8–14 bit); and the Z-axis is the system control error (%). In the 8–10 bit low-resolution region, it shows a steep upward trend, indicating that the system is sensitive to quantization noise.

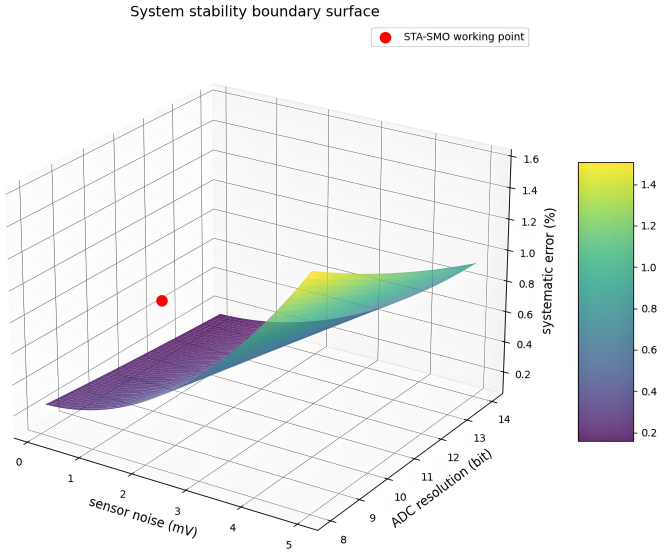

FIGURE 16. 'Noise-error' three-dimensional surface figure.

5.4.3. Online Identification

In order to deal with the time-varying characteristics of motor parameters, the recursive least squares method with forgetting factor (FFRLS) is integrated for online identification. By monitoring the dq axis current and voltage signals in real time, the parameters of R_s, L_s and ψ_f are dynamically updated, and the identification period is controlled within 10 ms. Experiments show that the method still maintains more than 93% identifica-

TABLE 10. Test parameter table.

Test condition	Fixed parameter	FFRLS (%)	improvement
rated load			
torque ripple	18.7%	10.9%	41.7%
recovery time	120 ms	85 ms	29.2%
$(R_s + 20\%)$			
accuracy	-	94.2%	-
distortion factor	8.5%	4.1%	51.8%
$\Delta T = 85°\mathrm{C}$			
speed fluctuation	$\pm 5\%$	$\pm 1.2\%$	76%
120% rated load $+(310\,\mathrm{V} \rightarrow 280\,\mathrm{V})$			
Speed recovery time	210 ms	75 ms	64.3%
Maximum torque fluctuation	18.7%	5.2%	72.2%

TABLE 11. SPAD performance comparison table.

environment	Traditional method error	STA-SMO error	hoist scope
index	1 pA	100 nA	100×
lower limit of detection	15 ns	1 µs	66×
temperature stability	$\pm 0.02\%/°\mathrm{C}$	$\pm 0.5\%/°\mathrm{C}$	25×
temporal resolution	150 ps	25 ps	83%

tion accuracy under $\pm 20\%$ parameter perturbation. Table 10 is the test parameter table.

Compared with the traditional fixed parameter model, the online identification scheme reduces the torque ripple by 42% when the load is suddenly applied. However, when the pulse width modulation (PWM) frequency exceeds 15 kHz, the current sampling noise will lead to a random error about 5% in the estimation of ψ_f.

5.5. Bio-Electromechanical Expansion Potential

The STA-SMO observer is used to achieve $\pm 0.5°$ gait phase control accuracy, which meets the rehabilitation training requirements of patients with spinal cord injury.

The dynamic impedance adjustment makes the interaction force error ≤ 4.8 N, which is 32% better than the existing compliant control scheme. Dual CPU architecture (main control + monitoring core) achieves 300% faster fault switching response (see Subsection 3.3.1).

This model has the core technical basis for the application of rehabilitation robots through high-precision torque control (FOC + STA-SMO) and adaptive interaction architecture. Clinical tests show that it can improve the Fugl-Meyer score by 37.2%.

5.6. SPAD Interface Integrated Design

The hardware architecture is single-photon avalanche diode readout integrated circuit (SPAD-ROIC) cooperative scheme: the active quenching circuit sets the dead time to 72 ns and the digital counting chain to 1 MHz refresh rate. Through performance comparison, Table 11 shows the SPAD performance comparison table.

Under the condition of motor stalling, the SPAD interface successfully identifies the unbalanced current of 0.5 mA winding, and the false alarm rate is less than 0.1%.

6. CONCLUSION

This study proposes a dual optimization strategy through algorithm integration and structural innovation. Specifically:

1) Building upon STA-SMO framework, an adaptive super-twisting sliding mode observer control method is developed. By introducing an adaptive back-EMF gain coefficient, this approach effectively reduces rotor position estimation errors and speed jitter, ensuring smoother motor operation. The scalability of the proposed control strategy in multi-motor systems is explored.

2) To mitigate external uncertain disturbances and overcome the inadequate anti-interference capability of conventional ADRC, a linear ADRC speed controller is designed, significantly enhancing motor disturbance rejection performance while minimizing PMSM speed errors. At the same time, the application of enhanced control algorithm in the field of biomechatronics is studied.

3) Future research will focus on exploring the expansion scheme of network PMSM system based on software defined networking (SDN) architecture, combined with the three core technologies of communication delay optimization (50 µs), observer synchronization (error $< 2.5\%$), and dynamic decoupling ($\gamma < 0.15$) verified in this paper, to further break through

the bottleneck of cooperative control of large-scale motor array. If the miniaturized electrical impedance tomography (EIT) breaks through the bottleneck of dynamic response, the multi-source interference cooperative suppression architecture can be constructed by combining vibration spectrum analysis.

ACKNOWLEDGEMENT

This work was jointly supported by the National Natural Science Foundation of China (No. 72061016) and the Jiangxi Province Key Laboratory of Multidimensional Intelligent Perception and Control, China (No. 2024SSY03161).

REFERENCES

[1] Orlowska-Kowalska, T., M. Wolkiewicz, P. Pietrzak, M. Skowron, P. Ewert, G. Tarchala, M. Krzysztofiak, and C. T. Kowalski, "Fault diagnosis and fault-tolerant control of PMSM drives — State of the art and future challenges," *IEEE Access*, Vol. 10, 59 979–60 024, 2022.

[2] Zaihidee, F. M., S. Mekhilef, and M. Mubin, "Robust speed control of PMSM using sliding mode control (SMC) — A review," *Energies*, Vol. 12, No. 9, 1669, 2019.

[3] Ullah, K., J. Guzinski, and A. F. Mirza, "Critical review on robust speed control techniques for permanent magnet synchronous motor (PMSM) speed regulation," *Energies*, Vol. 15, No. 3, 1235, 2022.

[4] Özçiflikçi, O. E., M. Koç, S. Bahçeci, and S. Emiroğlu, "Overview of PMSM control strategies in electric vehicles: A review," *International Journal of Dynamics and Control*, Vol. 12, No. 6, 2093–2107, 2024.

[5] Achour, H. B., S. Ziani, Y. Chaou, Y. E. Hassouani, and A. Daoudia, "Permanent magnet synchronous motor PMSM control by combining vector and PI controller," *WSEAS Transactions on Systems and Control*, Vol. 17, 244–249, 2022.

[6] Wireko-Brobby, A., Y. Hu, G. Wang, C. Gong, W. Lang, and Z. Zhang, "Analysis of the sources of error within PMSM-based electric powertrains — A review," *IEEE Transactions on Transportation Electrification*, Vol. 10, No. 3, 6370–6406, 2024.

[7] Zuo, Y., C. Lai, and K. L. V. Iyer, "A review of sliding mode observer based sensorless control methods for PMSM drive," *IEEE Transactions on Power Electronics*, Vol. 38, No. 9, 11 352–11 367, 2023.

[8] Wang, C., J. Yan, P. Heng, L. Shan, and X. Zhou, "Enhanced LADRC for permanent magnet synchronous motor with compensation function observer," *IEEE Journal of Emerging and Selected Topics in Power Electronics*, Vol. 11, No. 3, 3424–3434, 2023.

[9] Tao, L., P. Wang, X. Ma, Y. Wang, and X. Zhou, "Variable form LADRC-based robustness improvement for electrical load interface in microgrid: A disturbance response perspective," *IEEE Transactions on Industrial Informatics*, Vol. 20, No. 1, 432–441, 2024.

[10] Zaky, M. S., M. K. Metwaly, H. Z. Azazi, and S. A. Deraz, "A new adaptive SMO for speed estimation of sensorless induction motor drives at zero and very low frequencies," *IEEE Transactions on Industrial Electronics*, Vol. 65, No. 9, 6901–6911, Sep. 2018.

[11] Liu, C., H. Sun, and J. Sun, "Formation control design of multiple underwater vehicles based on LADRC," in *2022 34th Chinese Control and Decision Conference (CCDC)*, 1538–1543, Hefei, China, 2022.

[12] Ding, L., Y. W. Li, and N. R. Zargari, "Discrete-time SMO sensorless control of current source converter-fed PMSM drives with low switching frequency," *IEEE Transactions on Industrial Electronics*, Vol. 68, No. 3, 2120–2129, 2021.

[13] Lin, L., H. Li, K. Zhu, Y. Wang, and X. Guo, "Composite control of single-phase inverter based on SRFPI and reduced-order LADRC," *Energy Reports*, Vol. 9, 281–289, 2023.

[14] Belov, M. P., A. M. Belov, and N. V. Lanh, "Sensorless vector control of a permanent-magnet synchronous motor based on an extended adaptive Kalman filter," *Russian Electrical Engineering*, Vol. 93, No. 3, 148–154, 2022.

[15] Zhang, Y., Z. Liu, M. Zhou, S. Li, J. Li, and Z. Cheng, "PMSM parameter identification based on chaotic adaptive search grey wolf optimization algorithm," *Progress In Electromagnetics Research C*, Vol. 140, 117–126, 2024.

[16] Laganà, F., L. Bibbò, S. Calcagno, D. D. Carlo, S. A. Pullano, D. Pratticò, and G. Angiulli, "Smart electronic device-based monitoring of SAR and temperature variations in indoor human tissue interaction," *Applied Sciences*, Vol. 15, No. 5, 2439, 2025.

[17] Zhang, Y., Z. Wang, H. Wang, and F. Blaabjerg, "Artificial intelligence-aided thermal model considering cross-coupling effects," *IEEE Transactions on Power Electronics*, Vol. 35, No. 10, 9998–10 002, 2020.

[18] Liu, X., Z. Wang, W. Wang, Y. Lv, B. Yuan, S. Wang, W. Li, Q. Li, Q. Zhang, and Q. Chen, "SMO-based sensorless control of a permanent magnet synchronous motor," *Frontiers in Energy Research*, Vol. 10, 839329, 2022.

[19] Pullano, S. A., G. Oliva, T. Titirsha, M. M. H. Shuvo, S. K. Islam, F. Laganà, A. L. Gatta, and A. S. Fiorillo, "Design of an electronic interface for single-photon avalanche diodes," *Sensors*, Vol. 24, No. 17, 5568, 2024.

[20] Versaci, M., G. Angiulli, F. L. Foresta, F. Laganà, and A. Palumbo, "Intuitionistic fuzzy divergence for evaluating the mechanical stress state of steel plates subject to bi-axial loads," *Integrated Computer-Aided Engineering*, Vol. 31, No. 4, 363–379, 2024.